

Electric Field Distribution in strained p-i-n GaN/InGaN multiple quantum well structures.

A. N. Cartwright¹, Paul M. Sweeney¹, Thomas Prunty¹, David P. Bour² and Michael Kneissl²

¹Electrical Engineering, State University of New York at Buffalo, Buffalo, NY 14260,

²Xerox Palo Alto Research Center,

(Received Thursday, August 26, 1999; accepted Wednesday, October 20, 1999)

The presence of piezoelectric fields within *p-i-n* GaN/InGaN multiple quantum well structures is discussed. Time integrated and time-resolved photoluminescence measurements and theoretical calculations of the effect of these fields is presented. Furthermore, a description of how these fields influence the carrier dynamics and a discussion of how the piezoelectric field effects the design of GaN/InGaN devices is presented.

1 Introduction

III-N materials continue to be the focus of research on the development of UV/blue semiconductor optoelectronics [1] [2]. This is predominantly due to the success of Nakamura et. al at Nichia to develop blue semiconductor laser sources with lifetimes sufficient for incorporation into consumer optoelectronics [3] [4] [5] [6] [7]. With all of the attention paid to device operation, relatively little attention has focused on the fundamental properties of these materials. However, recently much interest has focused on the presence of piezoelectric fields within the quantum wells of $\text{In}_x\text{Ga}_{1-x}\text{N}/\text{GaN}$ heterostructures [8] [9] [10] [11]. More importantly, much research has focused on how the presence of this field will affect the design of devices based on this material.

It has been recently reported that these piezoelectric fields are quite large (between 300 to 800 kV/cm for 20 % Indium [10] [11]). This field is the direct result of the lattice mismatch between GaN and InN. The lattice constant of InGaN increases from that of GaN to the larger value of InN as the In content increases, resulting in compressive strain within the InGaN quantum well [11]. In addition, it has been shown that the piezoelectric electric field points toward the substrate for materials grown on a c-plane Sapphire substrate [11]. As we will demonstrate later, this is quite convenient for samples that are grown with n^+ GaN deposited on this substrate. Specifically, this orientation allows the built-in electric field of the *p-i-n* structure, E_{bi} , to partially compensate for the induced piezoelectric field.

In this paper, we provide some basic theoretical calculations and continuous wave and time-resolved photoluminescence experiments to demonstrate the effects of the piezoelectric field. We present a systematic approach of studying three samples with specific structures to verify the presence of the piezoelectric field. Specifically, we use a technique, that has been used successfully in work on (111) materials [12] [13] [14], to calculate the electric field within the quantum well for piezoelectric materials embedded within a *p-i-n* structure. Furthermore, we demonstrate that these calculations, and subsequent calculated band-structures, provide accurate descriptions for the observed behavior of InGaN/GaN *p-i*(MQW)-*n* samples under optical excitation. The calculated band-structures are used to discuss the expected carrier dynamics of these structures. Moreover, by following the variational calculation for energy levels and wave-functions in quantum well structures, following the work of Bastard [15], we calculate that in the InGaN/GaN material system the expected shift of excitonic wavelength caused by the piezoelectric field. These calculations of the reduction in oscillator strength predicts persistence of excitonic oscillator strengths to fields on the order of 1 MV/cm. Furthermore, this work experimentally demonstrates the expected increase in carrier lifetime due to the presence of the piezoelectric field. Moreover, while there have been previous experimental work that demonstrated an increase in carrier lifetime due to the piezoelectric field eg. [11], we demonstrate the effects of the built-in *p-i-n* field and the importance of a self-consistent model for calculating the in-well fields in these *p-i-n* structures

when interpreting the experimental results. This observation is in excellent agreement with recent theoretical calculations by Chow et al. [16] [17] where he predicts an optimum well width for minimizing lasing threshold. The experimental work focuses on time-integrated and time-resolved photoluminescence measurements as a function of pump power and excitation wavelength. The interpretation of the time-resolved PL is discussed in detail.

2 Growth of $\text{In}_x\text{Ga}_{1-x}\text{N}/\text{GaN}$ Structures

All samples in this work were grown using organometallic vapor phase epitaxy (OMVPE). The sample structure is shown in Figure 1. Growth was performed on a c-face (0001) sapphire substrate. Initially, a 4 micron thick layer of GaN:Si n-contact was deposited. This layer was followed by growth of the GaN barrier followed by an $\text{In}_x\text{Ga}_{1-x}\text{N}$ quantum well region. This barrier and quantum well region was repeated to achieve the desired number of quantum wells (2, 10, and 20 in the samples discussed here). The last quantum well was capped with a GaN barrier region followed by a GaN:Mg p-contact layer that varied from 0.2-1.0 microns. This results in an InGaN/GaN MQW region embedded within the intrinsic region of a *p-i-n* structure. The details of the layer thickness and In concentrations of the three samples studied in this work are presented in Table 1. The quantum well (QW) composition and thickness were estimated by x-ray diffraction, using the satellite reflections.

In order to calculate the bandstructure for these samples, the presence of the piezoelectric electric field within the heavily strained quantum well region must be included [18]. Specifically, it can be shown that, assuming the dielectric constant is the same for all constituent materials, the internal field distribution of *p-i(MQW)-n* structures must satisfy the following equations:

$$-(V_a + V_{bi}) = E_w L_w + E_b L_b \quad (1)$$

where V_a is the applied voltage, V_{bi} is the built-in electric field, E_w is the field within the well, L_w is the total width of the well material, E_b is the barrier field and L_b is the total width of the barrier material. In structures that contain piezoelectric fields within the quantum well material, the electric field within the quantum well can be written as:

$$E_w = E_p + E_{bi} \quad (2)$$

where E_p is the magnitude of the piezoelectric field within the strained well region given by [11]:

$$E_p = 2d_{31} \left(c_{11} + c_{12} + 2 \frac{c_{13}^2}{c_{33}} \right) \varepsilon_{xx} \quad (3)$$

where ε_{xx} is the in plane strain, c_{ij} are the elastic constants, and d_{31} is the piezoelectric constant.

Using these equations, it is possible to calculate accurate values for the fields within the barrier and the well regions. Moreover, these equations allow us to calculate the values of the field within these two regions under high excitation (E_{bi} is completely screened and $V_{bi} = 0$), and under dark conditions. In this work, we are interested in studying the fundamental properties of the materials without any applied electrical fields ($V_a = 0$) to complicate the modeling and data interpretation. Furthermore, we estimate the magnitude of the piezoelectric field by including the strain mismatch and piezoelectric constants and techniques described in the literature [19] [11]. The numerical results are shown in Table 2 for all samples with the applied voltage set to zero.

The resulting schematics of the calculated band-structure for the three samples under dark conditions with no applied voltage ($V_a = 0$) is shown in Figure 2. The band-structures of these materials are quite complicated. Specifically, this figure shows that there is an overall envelope field due to the *p-i-n* structure (E_{bi}). In addition, because of the compressive strain within the quantum well region, the piezoelectric field within these structures points toward the substrate and therefore opposes the built-in electric field. Notice, that it is possible for the well and barrier regions to see drastically different electric fields. The results presented above rely on an accurate value for the piezoelectric field. Here, we have used previously determined values from the literature [11] [19]. Finally, if the piezoelectric field is not present, the expected shift in excitonic resonance by screening the built-in *p-i-n* field would be expected to be largest in B2, and smallest in B20. However, in contrast, when we include the piezoelectric electric field, the shift of the excitonic resonance is expected to be largest in B2 and B20 and smallest in B10.

3 Expected Carrier Dynamics

From this data and from our previous studies of piezoelectric (111) samples and *p-i-n* structures [14] [20] [21] [22], we can discuss a number of time-scales where certain carrier transport issues dominate. Specifically, we can discuss time constants associated with the following phenomena: (a) τ_{perp} perpendicular transport, (b) τ_{R} excitonic (in-well) recombination, (c) τ_{yl} yellow

band emission, (d) τ_{SS} recombination of spatially separated carriers, and (e) τ_D diffusion of carriers in the n and p regions. All of these phenomena occur simultaneously, however there are time regimes where particular carrier dynamics dominate. Specifically, we expect the perpendicular transport to be very short, a few picoseconds, because it only involves the transport of electrons and holes from the intrinsic region to the doped region under the influence of the built-in $p-i-n$ electric field. Moreover, it has been found that the radiative recombination time of carriers in InGaN quantum well structures are typically between a few hundred picoseconds and a few nanoseconds [23] [24] [25] [26] [27]. Furthermore, using a simple theory it can be shown that the recombination of the spatially separated carriers (carriers that are confined to the doped regions by the built-in $p-i-n$ field) in these $p-i-n$ structures can be as long as seconds [28]. Finally, it is well established that typical decay times of milliseconds has been observed for the yellow emission. With these estimates, it is reasonable assumption to assume that $\tau_{perp} < \tau_D < \tau_R < \tau_{yl} < \tau_{SS}$.

In these structures, with no applied electrical bias, the carrier dynamics should be expected to follow the following general description. Photogenerated carriers generated within the intrinsic region of the $p-i-n$ will drift to the doped regions under the influence of the built-in electric field. If there is sufficient power in the pump source, this process will continue until the built-in field is completely screened. Once the built-in electric field is completely screened, any excess carriers generated within the intrinsic region will remain in this area and can contribute to direct recombination (excitonic emission) within the quantum wells. This direct recombination will continue as long as there are still sufficient carriers remaining to screen the built-in electric field. Note, that the in-well field is drastically changed by the screening of the built-in electric field (as shown in Table 2). Any excess carriers screen the electric field within the quantum well returning the quantum well to flat band conditions and increasing the oscillator strength of the excitonic transition [16] [17]. The theoretical treatment and experimental demonstration of this mechanism is well established for (111) InGaAs/GaAs piezoelectric $p-i-n$ structures [14] [20] [29] [30] [21] [22].

Once a sufficient number of the photogenerated carriers have recombined, the carrier dynamics from this time forward are similar to conditions of low fluence incident on the sample. Specifically, if there is not sufficient power (and therefore not sufficient photogenerated carriers) to completely screen the built-in electric field, the majority of the carriers will drift to the doped region

and become spatially separated by the presence of this built-in electric field. The percentage of the photogenerated carriers that arrive at the doped regions is directly proportional to the respective rates of the perpendicular transport, diffusion, and all sources of recombination. Chow et al. have theoretically demonstrated that the spatial separation of the carriers within the quantum well lead to an increase in the carrier lifetimes [16] [17]. In a similar manner, we have previously demonstrated that, for sufficiently low carrier densities (where the $p-i-n$ field is not completely screened), the carriers within a $p-i-n$ structure are strongly confined to the doped regions by the built-in electric and, therefore, exhibit drastically elongated carrier lifetimes [28]. In $p-i-n$ structures, the electrons and holes have a reduced overlap integral and therefore exhibit longer effective recombination times. More importantly, if the carriers are spatially separated and confined to the doped regions within the $p-i-n$ structures, we would expect yellow emission from the doped regions to be a direct indicator of the presence of these spatially separated carriers.

Subsequently, the carriers will decay in the doped regions by either yellow emission from the carriers confined in the doped regions or through diffusion in the plane of the doped regions. Once the carriers begin to decay, the space charge field generated by these photogenerated carriers begins to decrease. Consequently, the screening of the built-in electric field decreases. In this way, the remaining carriers are more strongly confined to the doped regions, resulting in an increase in the effective recombination time. We propose that most of the recombination of these carriers, based on our simple models and experimental results, contributes to the yellow emission. Moreover, the diffusion within the plane of the doped regions is directly proportional to the gradient of the carrier distribution. Therefore, more tightly focused spots should diffuse more rapidly, resulting in more carriers being more tightly confined. Thus, the exact behavior of the carriers is a complicated coupled system that needs to be accurately modeled.

4 Variable Pump Photoluminescence

In order to verify the aforementioned carrier dynamics, photoluminescence (PL) studies of these structures were conducted for different incident pump powers, pump wavelengths and spot sizes. The experimental arrangement of the photoluminescence experiment is as shown in Figure 3. The pump source was the frequency doubled output from a tunable mode-locked Ti:Sapphire laser that typically produced 20 mW of ~200 fs pulses with a repetition rate of 80 MHz tunable from 360 to 420 nm. This light was mechanically chopped at a frequency of 2 kHz. The frequency doubled light from the Ti:Sapphire was focussed onto the sample. In order to

observe any effects for in-plane diffusion in the n- and p-doped regions, we adjusted the distance from the focusing lens to the sample and monitored the laser spot-size with a Thorlabs Omega meter. The resulting photoluminescence from the sample was collected by a focusing lens that focused it onto the entrance slit of a computer controlled scanning monochromator. The output from the monochromator was detected using a photodiode and standard lock-in techniques. Moreover, the power incident on the sample was varied by introducing neutral density (ND) filters in the path of the incident pump beam allowing the pump power to be varied from 20mW to a few micro-Watts. In addition, the tunability of the Ti-sapphire laser allowed the wavelength of the incident frequency doubled light to be varied. In this work we focused on using ~ 200 fs pulses with central pump wavelengths of 370 nm (allowing overlap of the excitation spectra with the bandgap of the GaN material) and 400 nm (transparent to the GaN layers but absorbed within the InGaN wells) with approximately 10 nm of bandwidth. With this setup these measurements could be performed for various pump power, pump wavelength, and pump spot-size. For the following discussion of time-integrated photoluminescence, all data was acquired at room temperature.

5 Results and Discussions

The above description of expected behavior makes the interpretation of the data relatively easy. Figure 4 shows the integrated photoluminescence for the two quantum well sample, B2, with a pump wavelength of 370 nm. Both excitonic emission at 450 nm and yellow emission centered at 550 nm is evident. Notice that as the incident fluence decreases, the yellow emission increases (relative to the excitonic emission). This is a result of the technique used for decreasing the fluence. In these experiments we increased the spot size while keeping the incident power constant. In this way, the total integrated number of carriers within the sample remained constant for all fluence levels (they are simply spread over a larger area). Recall that the photogenerated carriers are more strongly confined for smaller space charge fields. Consequently, lower fluences that result in lower space charge fields give rise to better carrier confinement in the doped regions. As stated earlier, the yellow emission occurs within the *n*-doped regions. Therefore, better carrier confinement means that it is more likely for the carriers to be in the doped regions and more likely to decay through the yellow emission.

Figure 5 shows a similar set of data for the 10 quantum well sample, B10, and Figure 6 shows a similar set of data for the 20 quantum well sample, B20. In both cases the behavior is quite similar to that of B2. However, the excitonic emission line-width is much nar-

rower. We believe that the emission of B2 is much broader due to the relatively low confinement of the hole state in the valence band of the quantum well (see Figure 2). Moreover, this sample has very large fields in the quantum well under dark and high excitation conditions (varying from -400 kV/cm in dark conditions to 700 kV/cm under high excitation). Therefore, both electron and hole wave-functions are broadened to include the increased probability that the carrier can tunnel through the sharply tilted barrier. As should be expected by observing Figure 2, this probably is much higher for the hole in the valence band of the quantum well. By contrast, the hole states in both B10 and B20 have a "thicker" barrier to tunnel through because of the slope of the built-in electric field. Thus, both B10 and B20 have a narrower excitonic emission. Moreover, these samples also have sufficiently large in-well electric fields that significantly broaden the emission through the quantum confined Stark effect. Finally, notice that the necessary fluence required for the excitonic emission to be larger (in peak value) than the yellow emission is directly proportional to the magnitude of the built-in electric field in each sample.

Finally, we show in Figure 7, a composite of the results for excitation of the samples with the pump tuned to 400 nm. In this figure, we show the resulting PL intensity as a function of the distance from the center of the excitonic emission ($\lambda - \lambda_0$). A few features are worth noting. Firstly, this wavelength is only absorbed within the quantum well material. As such, few carriers are generated since these thicknesses are quite low. In addition, the energy of this light creates carriers that are well confined within the quantum well material and do not easily escape the quantum well to drift to the doped regions and contribute to yellow emission. In all of the data for these samples with a pump wavelength of 400 nm, there was little evidence of yellow emission. Secondly, because all of the curves shown in Figure 7 are for approximately the same fluence level, it should be expected that the photoluminescence intensity should be proportional to the total quantum well thickness (provided that all other experimental variations remained the same). We observe ratios of 1:6.2:9.9 for the PL intensity for the 2:10:20 quantum well structures, respectively, with total quantum well length ratios of 1:5.3:10. The small discrepancy in the 2 to 10 quantum well sample is easily explained by the difference in the observed line-width of the emission of the light. As we have demonstrated in the past, we expect the product of the amplitude of absorption and the line-width of the excitonic absorption to remain a constant [31]. Therefore, it is reasonable to assume that the amplitude of emission and the line-width of the excitonic emission should remain a constant.

6 Time Resolved Photoluminescence

The previous sections focused on the time-integrated photoluminescence. The experimental determination of the behavior of time-integrated photoluminescence was necessary for a better understanding of the time-resolved photoluminescence spectra from these samples. Figure 8, shows the time-resolved photoluminescence experiment. The frequency doubled output from a Ti:Sapphire laser is that produces pulses at a repetition rate of 80 MHz is used as the pump source. The resulting photoluminescence is imaged onto the entrance slit of the Hamamatsu streak camera and the streak camera is triggered synchronously with the repetition rate of the laser pulses. In addition, a delay generator is used to temporally position the triggering of the streak camera monitor any time slice of the emitted photoluminescence. In order to maximize the intensity of the photoluminescence and to narrow the excitonic emission and increase our chances of time-resolving shifts in the excitonic emission, all time-resolved data presented here were acquired at 15K.

A simple calculation, following the work of Bastard [15], can be used to estimate the transition energy and the energy shift with the in-well field of samples B10 and B20. Sample B2 follows a similar curve as B20. Figure 9 shows the resulting curves for the quantum confined Stark effect shift for varying conduction band offsets from 0.6 to 0.8 for these two samples. Notice that, for similar in-well fields, the change in transition energy is expected to be smaller in sample B20 than sample B10. However, from Table 2, sample B10 has a smaller piezoelectric field than sample B20. Furthermore, notice that Figure 9 can be used to estimate the shift given the calculated fields from Table 2. For sample B10 (with an in-well field of 400 kV/cm) we expect between a 15 to 25 meV shift and for sample B20 (in-well field of 630 kV/cm) and sample B2 (in-well field of 700 kV/cm) we expect between a 25 to 35 meV shift (dependent on the value of the conduction band offset).

The resulting spectral curves for sample B10 is shown in Figure 10. The results are consistent with the models that were proposed earlier. Specifically, at short times after the pump excitation, the carriers drift to screen the built-in electric field (due the $p-i-n$). Once this field is screened the excess carriers generated within the intrinsic region and quantum wells remain in this region and can serve to screen and saturate the excitonic emission. As shown in Figure 10, the excitonic emission shifts to higher energy for short times. As time increases, the carriers recombine and the screening decreases. This decrease in screening is shown by the shift in the excitonic emission toward lower energies

and the carriers recombine. Notice that the shift from 1ns to 11 ns is approximately 10 meV. This shift fits well within the calculated values given in Figure 9. Moreover, the identical experiment was performed on samples B20 and B2. The results for sample B20 are shown in Figure 11. As expected, the behavior of the sample is identical to sample B10 except that the magnitude of the shift is larger (approximately 30 meV). In addition, the observed shift in sample B2 was approximately 30 meV.

Finally, Figure 12 shows the lifetimes of emission at different energies for sample B20. It is obvious that the lifetime is shorter for the higher energy transitions. This is consistent with a model for the field induced lifetime elongation due to spatial separation of the electron and hole wavefunctions [16] [17]. Specifically, this sample showed a high energy (flat band) emission lifetime of approximately 500 picoseconds whereas the low-energy emission (piezoelectric field not screened) showed a lifetime as long as 5 ns. Thus, we see that the presence of the piezoelectric field has increased the lifetime of the carriers and would decrease the total number of carriers that are necessary to create population inversion. Chow et al. have performed this calculation and demonstrated that there should be an optimum well width (and corresponding elongated carrier lifetimes) for lower laser threshold currents. Here, we believe that one must include the indium concentration and intrinsic region width (field distributions) in these laser threshold current calculations.

7 Summary

We have demonstrated a simple model that includes the piezoelectric field when calculating the in-well electric field in InGaN/GaN $p-i(MQW)-n$ structures. With this model we have shown that the built-in electric field compensates for the piezoelectric field, but because of the extreme magnitude of the piezoelectric field, the quantum wells are always under very large electric field conditions. This in-well field causes the wave functions of the electrons and holes to be bunched toward opposite sides of the wells and reduces the overlap of the electron and hole wave-functions resulting in a reduction of the oscillator strength for the excitonic emission (by about a factor of two). However, experimentally we have shown that the lifetimes of the carriers within these structures increases drastically as the piezoelectric field recovers from initial screening at short times (see Figure 12 above). The development of composite structures (with varying well widths, indium concentration, etc.) that maximize the lifetimes and gain for optimum lasing conditions should be the emphasis of future work on developing lasing structures. We find these measurements to be consistent with the recent calculations of

Chow et al. [16] [17] that predict a large increase in carrier lifetimes along with a small reduction in gain. Furthermore, we expect an optimum well width that should reduce the threshold current of lasers, but we also expect an optimum indium concentration and distribution of the wells within the intrinsic region.

Moreover, the development of composite structures that can accurately control the in-well field will result in devices geometries for visible spatial light modulators for the visible wavelength range. Future work will focus on more accurate modeling and the development of composite structures for better laser and modulator operation.

ACKNOWLEDGMENTS

The authors wish to acknowledge the support of the National Science Foundation CAREER award #9733720 and Dr. Tien P. Lee of the National Science Foundation for his helpful suggestions and discussions.

REFERENCES

- [1] S. Nakamura, *J. Cryst. Growth* **170**, 11-15 (1997).
- [2] D. P. Bour, M. Kneissl, L. T. Romano, M. D. McCluskey, C. C. Van deWalle, B. S. Krusor, R. M. Donaldson, J. Walker, C. J. Dunnrowicz, N. M. Johnson, *IEEE J. Selected Topics Quantum Electron.* **4**, 498 (1998).
- [3] S. Nakamura, M. Senoh, S. Nagahama, N. Iwasa, T. Yamada, T. Matsushita, H. Kiyoku, Y. Sugimoto, T. Kozaki, H. Umemoto, M. Sano, K. Chocho, *Jpn. J. Appl. Phys.* **37**, L309 (1998).
- [4] S. Nakamura, *Mater. Res. Bull.* **23**, 37 (1998).
- [5] S. Nakamura, M. Senoh, S. Nagahama, N. Iwasa, T. Yamada, T. Matsushita, H. Kiyoku, Y. Sugimoto, T. Kozaki, H. Umemoto, M. Sano, K. Chocho, *Jpn. J. Appl. Phys.* **37**, L627 (1998).
- [6] S. Nakamura, *IEEE J. Quantum Electron.* **4**, 483 (1998).
- [7] S. Nakamura, M. Senoh, S. Nagahama, N. Iwasa, T. Yamada, T. Matsushita, H. Kiyoku, Y. Sugimoto, T. Kozaki, H. Umemoto, M. Sano, K. Chocho, *Appl. Phys. Lett.* **73**, 832 (1998).
- [8] T. Deguchi, A. Shikanai, K. Torii, T. Sota, S. Chichibu, S. Nakamura, *Appl. Phys. Lett.* **72**, 3329 (1998).
- [9] W. Liu, K. L. Teo, M. F. Li, S. J. Chua, K. Uchida, H. Tokunaga, N. Akutsu, K. Matsumoto, *J. Cryst. Growth* **190**, 648 (1998).
- [10] S. F. Chichibu, A. C. Abare, M. S. Minsky, S. Keller, S. B. Fleischer, J. E. Bowers, E. Hu, U. K. Mishra, L. A. Coldren, S. P. DenBaars, T. Sota, *Appl. Phys. Lett.* **73**, 2006 (1998).
- [11] Andreas Hangleiter, Jin Seo Im, H. Kollmer, S. Heppel, J. Off, Ferdinand Scholz, *MRS Internet J. Nitride Semicond. Res.* **3**, 15 (1998).
- [12] J. L. Sanchezrojas, A. Sacedon, A. Sanzhervas, E. Calleja, E. Munoz, E. J. Abril, M. Aguilar, M. Lopez, *Semicond. Sci. Technol.* **10**, 1173 (1995).
- [13] J. L. Sanchezrojas, A. Sacedon, F. Calle, E. Calleja, E. Munoz, *Appl. Phys. Lett.* **65**, 2214 (1994).
- [14] X. R. Huang, D. R. Harken, A. N. Cartwright, A. L. Smirl, J. L. Sanchezrojas, A. Sacedon, E. Calleja, E. Munoz, *Appl. Phys. Lett.* **67**, 950 (1995).
- [15] G. Bastard, E. E. Mendez, L. L. Chang, L. Esaki, *Phys. Rev. B* **26**, 1974 (1982).
- [16] W. Chow, M. Kira, S. W. Koch, *Phys. Rev. B* **68**, 1947 (1999).
- [17] W. W. Chow, H. Amano, T. Takeuchi, J. Han, *Appl. Phys. Lett.* **75**, 244 (1999).
- [18] A. S. Pabla, J. L. Sanchezrojas, J. Woodhead, R. Grey, J. P. R. David, G. J. Rees, G. Hill, M. A. Pate, P. N. Robson, R. A. Hogg, T. A. Fisher, A. R. K. Willcox, D. M. Whittaker, M. S. Skolnick, D. J. Mowbray, *Appl. Phys. Lett.* **63**, 752 (1993).
- [19] Christian Wetzel, Shugo Nitta, Tetsuya Takeuchi, Shigeo Yamaguchi, H. Amano, I. Akasaki, *MRS Internet J. Nitride Semicond. Res.* **3**, 31 (1998).
- [20] A. N. Cartwright, D. S. McCallum, T. F. Boggess, A. L. Smirl, T. S. Moise, L. J. Guido, R. C. Barker, B. S. Wherrett, *J. Appl. Phys.* **73**, 7767 (1993).
- [21] X. R. Huang, D. R. Harken, A. N. Cartwright, D. S. McCallum, A. L. Smirl, J. L. Sanchezrojas, A. Sacedon, F. Gonzalezsan, E. Calleja, E. Munoz, *J. Appl. Phys.* **76**, 7870 (1994).
- [22] X. R. Huang, A. N. Cartwright, D. R. Harken, D. S. McCallum, A. L. Smirl, J. L. SanchezRojas, A. Sacedon, E. Calleja, E. Munoz, *J. Appl. Phys.* **79**, 417 (1996).
- [23] J. Allegre, P. Lefebvre, W. Knap, J. Camassel, Q. Chen, M. A. Khan, *MRS Internet J. Nitride Semicond. Res.* **2**, 34 (1997).
- [24] C. K. Sun, T. L. Chiu, S. Keller, G. Wang, M. S. Minsky, S. P. DenBaars, J. E. Bowers, *Appl. Phys. Lett.* **71**, 425 (1997).
- [25] W. Li, P. Bergman, B. Monemar, H. Amano, I. Akasaki, *J. Appl. Phys.* **81**, 1005-1007 (1997).
- [26] CK Sun, S. Keller, G. Wang, MS Minsky, JE Bowers, SP DenBaars, *Appl. Phys. Lett.* **69**, 1936-1938 (1996).
- [27] T. Wang, D. Nakagawa, J. Wang, T. Sugahara, S. Sakai, *Appl. Phys. Lett.* **73**, 3571 (1998).
- [28] A. N. Cartwright, "Nonlinear optical properties of hetero *n-i-p-i* device structures", Thesis in *Electrical and Computer Engineering*. Iowa City: University of Iowa, (1995)
- [29] M. Livingstone, I. Galbraith, B. S. Wherrett, *Appl. Phys. Lett.* **65**, 2771 (1994).
- [30] M. Livingstone, I. Galbraith, B. S. Wherrett, *Nuov. Cim. D* **17**, 1595 (1995).
- [31] A. N. Cartwright, X. R. Huang, A. L. Smirl, *IEEE J. Quantum Electron.* **31**, 1726 (1995).

FIGURES

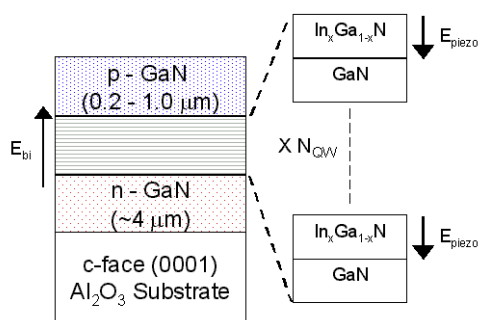


Figure 1. Schematic of the structures of the GaN/InGaN *p-i-n* samples used in this study.

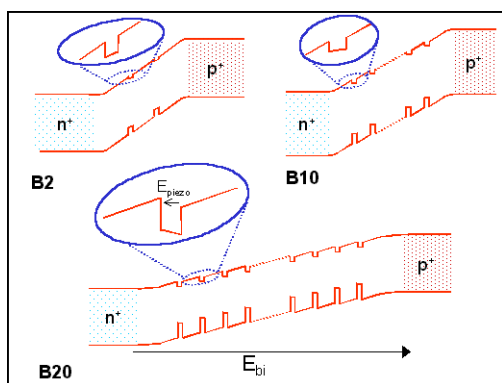


Figure 2. Calculated bandstructures for the three samples studied in this work. This figure shows the directions of the built-in electric field, E_{bi} , and the piezoelectric electric field, E_{piezo} . Notice that the piezoelectric field within the quantum well opposes the built-in electric field.

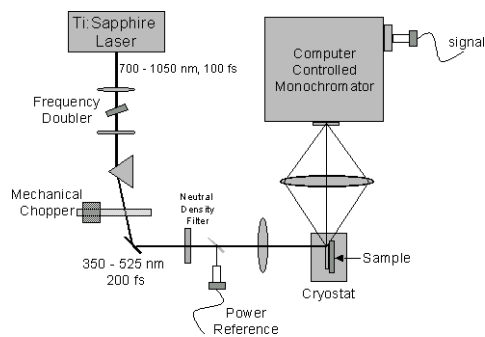


Figure 3. Time-integrated photoluminescence set-up. The frequency doubled output of a femtosecond Ti:Sapphire laser is used as the pump source. Standard lock-in techniques are used to improve signal to noise ratio. The samples were edge emitting due to the waveguiding of the GaN buffer layers.

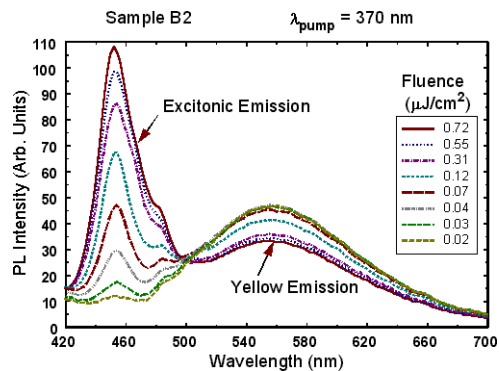


Figure 4. Time-integrated photoluminescence for sample B2. In this case, the frequency doubled output of the femtosecond Ti:Sapphire laser is tuned to 370 nm. Clearly, excitonic emission centered at 450 nm is present. In addition, sufficient overlap of the pump wavelength and the absorption edge of GaN was present. The yellow emission is from Ga vacancies within the n-doped material and served as a marker for the presence of carriers for screening of the built-in electric field.

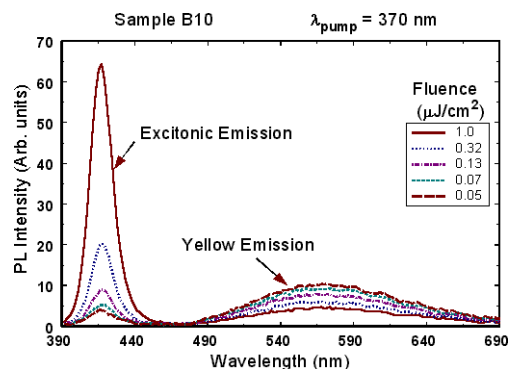


Figure 5. Time-integrated photoluminescence for sample B10 with the pump tuned to 370 nm. Clearly, excitonic emission centered at 411 nm is present. Again, the yellow emission is clearly visible, however excitonic emission dominates at a lower fluence.

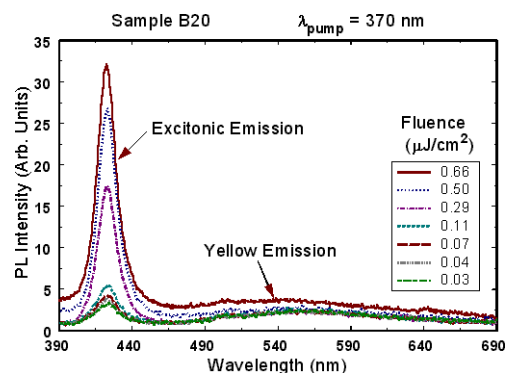


Figure 6. Time-integrated photoluminescence for sample B20 with the pump tuned to 370 nm. Excitonic emission was centered at 424 nm. The yellow emission is still present but less than that of the previous two samples.

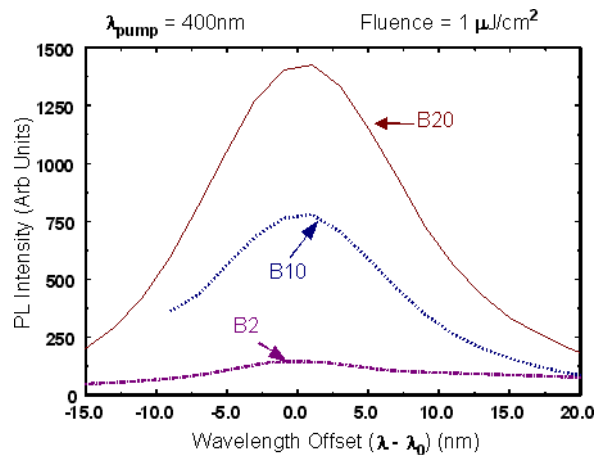


Figure 7. Time-integrated photoluminescence for all three samples for the same fluence. In this case, the frequency doubled output of a femtosecond Ti:Sapphire laser was tuned to 400 nm. This pump wavelength was sufficiently long to be absorbed only by the quantum well material. As expected, the PL intensity is proportional to the total length of the quantum wells within the intrinsic region. There was no evidence of yellow emission for the carrier densities excited with the given fluence at 400 nm.

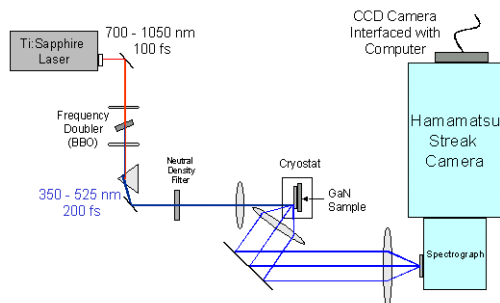


Figure 8. Time-resolved photoluminescence using a Hamamatsu C4334 streak camera. As in the time-integrated photoluminescence, the frequency doubled output of a femtosecond Ti:Sapphire laser is used as the pump source. The streak camera is triggered synchronously with the pulses from the Ti:Sapphire.

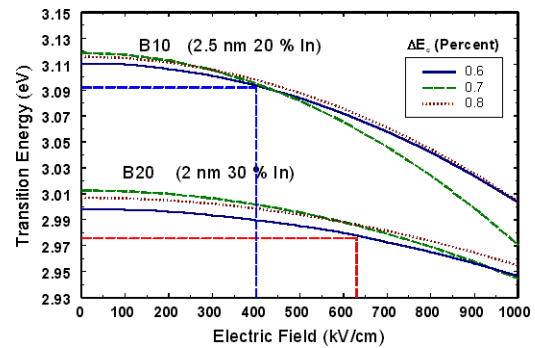


Figure 9. Calculated excitonic transition energies and shift of excitonic transition energy versus in-well field for samples B10 and B20 for conduction band offsets varying from 0.6 to 0.8.

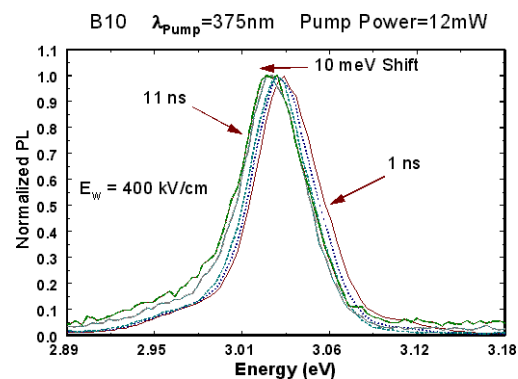


Figure 10. Time-resolved photoluminescence spectra for sample B10 at 15K with pump power of 12 mW and pump wavelength of 375 nm. There is an observed shift of ~10 meV.

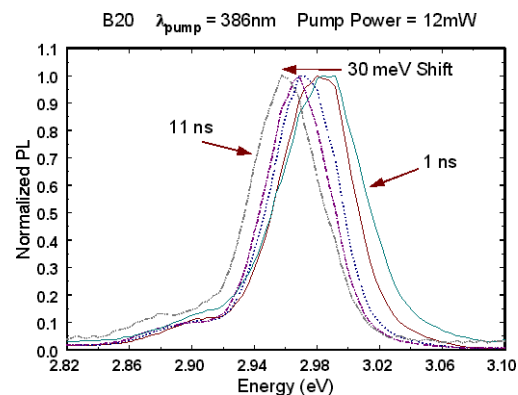


Figure 11. Time-resolved photoluminescence spectra for sample B20 at 15K with pump power of 12 mW and pump wavelength of 386 nm. There is an observed shift of ~30 meV.

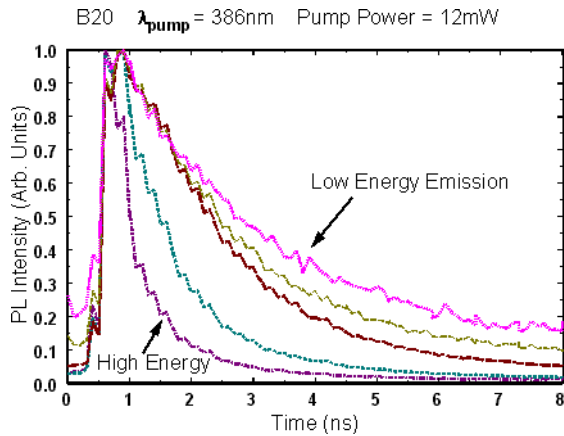


Figure 12. Temporal resolution of emission lifetimes for different emission energies for sample B20. The high energy emission is the expected emission with no in-well field. Notice that the lifetime is significantly shorter.

Table 2. Calculated built-in electric field, barrier field and quantum well field under dark conditions and high excitation conditions using a simple model that includes the effect of the piezoelectric field within the quantum well (units are kV/cm). The in-well electric field is always sufficiently large to decrease the oscillator strength for the excitonic transition.

Sample	Dark Condition			High Excitation	
Fields in kV/cm	E_{bi}	E_b	E_w	E_b	E_w
B2	1100	-1200	-400	-100	700
B10	380	-470	90	-140	420
B20	180	-350	450	-170	630

TABLES

Table 1. Specific structure values for the $p-i(MQW)-n$ structures. In this table L_B is the thickness of the barrier region, L_w is the thickness on the well region, x is the Indium concentration, and N_w is the number of quantum wells in the intrinsic region.

Sample	N_w	$x(\%)$	$L_w(\text{\AA})$	$L_B(\text{\AA})$
B2	2	30	20	90
B10	10	20	25	70
B20	20	30	20	70